INTERNATIONAL JOURNAL FOR NUMERICAL METHODS IN FLUIDS, VOL. 19, 981–995 (1994)

PRESSURE-BASED METHOD FOR COMBUSTION INSTABILITY ANALYSIS

Y. M. KIM

Hanyang University, Seoul 133-791, South Korea

AND

Z. J. CHEN, C. P. CHEN*, AND J. P. ZIEBARTH

University of Alabama in Huntsville, Huntsville, AL 35899, U.S.A.

SUMMARY

An improved pressure-based method has been applied to predict the two-dimensional instability analysis of liquid-fuelled rocket engines. This method is non-iterative for transient flow calculations and applicable to all-speed flows. Validation cases include the shock-tube problem, the blast flow field and unsteady spray-combusting flows. Computations for the combustion instability analysis were carried out for various combustion parameters such as spray initial conditions and combustor geometries. Unsteady behaviours of the stable and unstable spray flame fields and effects of acoustic oscillations on the fuel droplet vaporization and combustion process are studied in detail. The present numerical model successfully demonstrates the capability of predicting combustion instability as well as fast transient compressible flows at all speeds.

KEY WORDS Pressure-based method All-speed Blast wave Two-phase flow Combustion instability

1. INTRODUCTION

Combustion instability in liquid-fuelled rocket engines has long been a matter of serious practical concern. Combustion instability can be driven by non-linear interactions among acoustic waves and complex physical processes such as atomization, vaporization, vortex shedding, turbulent mixing and chemical reaction. Owing to this complex nature of combustion instability, the analysis of acoustic amplification by overall combustion processes is an extremely difficult task. In practice a variety of approximations have been made to simplify the analysis. However, it is always acknowledged that numerical integrations of the transient Navier–Stokes equations coupled with relevant physical submodels will provide the ultimate solutions.

The computational methods for solving the transient Navier–Stokes equations are largely classified as either density-based methods or pressure-based methods. These two methodologies have their own advantages and disadvantages in simulating transient high-speed flows and handling low-Mach-number viscous flows. The basic merit of the density-based method is its accuracy and robustness, especially for transient high-speed flow simulation. However, the density-based algorithm is often ineffective for low-Mach-number flows owing to the stiff eigenvalues of the system. The density-based method breaks down completely at the incompressible limit where density is independent of pressure and the pressure term in the momentum equations

* Author to whom correspondence should be addressed.

CCC 0271–2091/94/230981–15

Received 6 October 1992
Revised 13 April 1994

become singular. In the pressure-based method the pressure–density–velocity coupling is handled by a Poisson-type pressure or pressure correction equation derived from the continuity and momentum equations and an equation of state. As a result, the pressure-based algorithm is relatively easy to apply to flows of all speeds. Since the pressure-based method usually employs a sequential solution procedure, it requires less computer memory and less computing time. However, the pressure-based method has difficulties accounting for all wave propagation properties in transient compressible flows, because the upwinding procedure of the pressure-based method is usually based on physical velocities rather than characteristic velocities. There have been several research efforts[1–5] to develop pressure-based methods for fast transient flow calculations. In the present study a pressure-based method has been developed for handling the strong non-linear couplings arising in multiphase, fast transient and reacting flows. The present procedure is basically similar to the non-iterative PISO algorithm[4] recently proposed by Issa *et al.* However, the present approach allows us to consistently discretize the momentum equations with reduced splitting errors. To reflect the rapid and large variations in density, temperature and mass fractions, the scalar conservation equations such as species, energy and turbulent transport quantities are solved in the same predictor–corrector sequence, with the coefficient matrices being updated in the corrector steps. This method is non-iterative and applicable to all-speed flows.

To assess and demonstrate the predictive capabilities of the present solution algorithm, the shock-tube problem, the blast flow field and the combustion instability of liquid propellant rocket engines are selected as example problems. Computations were carried out for various combustion parameters such as spray initial conditions and combustor geometries (combustor length, nozzle length of converging section).

2. PHYSICAL MODELS

The mathematical formulation of the two-phase flow and combustion processes utilizes the Eulerian conservation equation for the gas phase and the Lagrangian equation for the fuel droplets. The two-way coupling between the two phases is described by the exchange rate terms which represent the rates of momentum, mass and heat transfer. For liquid rocket applications a strongly coupled procedure[6] to handle the highly evaporating spray-combusting flows has been implemented. The solution of the dispersed liquid droplet equations formulated on a Lagrangian frame is embedded within the non-iterative predictor–corrector solution procedure. The current two-phase solution procedure[6] has been proved to be efficient and has shown advantages over others such as the particle-source-in-cel (PSIC) algorithm[7] and the ALE-ICE algorithm.[8]

Gas phase equations

The density-weighted conservation equations of mass, momentum and scalar variables expressed in a Eulerian co-ordinate frame can be written as

$$\frac{\partial \rho}{\partial t} + \frac{\partial}{\partial x_i}(\rho u_i) = S_{m,l}, \tag{1}$$

$$\frac{\partial \rho u_i}{\partial t} + \frac{\partial}{\partial x_j}(\rho u_i u_j) = -\frac{\partial p}{\partial x_i} - \frac{\partial p}{\partial x_j}(\rho \overline{u_i' u_j'}) + S_{u_i,l}, \tag{2}$$

$$\frac{\partial \rho \phi}{\partial t} + \frac{\partial}{\partial x_i}(\rho u_i \phi) = -\frac{\partial}{\partial x_i}(\rho \overline{u_i' \phi'}) + S_\phi + S_{\phi,l}, \tag{3}$$

where ρ is the time-mean density of the mixture, u_i and u_i' are the ith components of the density-weighted mean and fluctuating part of the instantaneous velocity respectively, ϕ and ϕ' are the density-weighted mean and fluctuating part of instantaneous scalar quantities respectively (including the species concentrations and the internal energy), p is the mean pressure and S_ϕ and $S_{\phi,l}$ represent the gas phase source terms and the interaction source terms due to the fuel spray respectively. Detailed expressions for these source terms can be found in Reference 9. In the present study the unknown turbulent correlations, $\overline{u_i'u_j'}$ and $\overline{u_i'\phi'}$ are modelled by the two-equation turbulent diffusivity model.[10] Based on an irreversible single-step chemical reaction, the reaction rate in the spray flame is determined from either the mixing rates[11] of the reactants or the chemical reaction rate[12] of the Arrhenius type, whichever is slower.

Droplet phase equations

The spray dynamics is described by a discrete particle-tracking method formulated on a Lagrangian frame. This is essentially a statistical approach and requires a sufficiently large number of computational particles for realistic representation of sprays. Each computational particle represents a number of droplets having equal location, velocity, size and temperature. Mean gas phase properties and instantaneous eddy properties are used for the stochastic droplet-tracking calculations. The droplet evaporation rates are given by the Frossling correlation[13] and the transient droplet temperatures are obtained by the infinite conductivity model.[14] The major assumptions and detailed formulations in the droplet transport calculations can be found in References 14 and 15. The correct evaluation of the average physical properties in the gas film is of importance in the vaporization calculations. In accordance with Hubbard *et al.*'s recommendations,[16] the 'one-third rule' has been used in the present study. The variable thermophysical properties such as fuel vapour pressure are estimated from the JANNAF databank.[17]

Turbulence/droplet interactions

In the spray system the gas and dispersed droplets interact with each other at both mean and fluctuational levels. At the fluctuational level the droplets experience dispersion due to the action of the turbulence field, while the turbulence field itself experiences a modulation effect due to the particles. Since the present study deals with dilute dispersed flows, we did not consider dense spray effects such as turbulence modulation, drop break-up and collision. The two-way coupling between gas and droplets involves interactions at both mean flow field and fluctuational levels in turbulent flows. The turbulence effects on droplet dispersion are simulated by a Monte-Carlo method and random turbulent fluctuating velocity components are assumed to have a Gaussian probability distribution with standard deviation based on the turbulent kinetic energy. The instantaneous velocity components are obtained by adding stochastically generated turbulent fluctuating velocity components to the mean gas phase velocity field. This type of simulation for the turbulent dispersion of droplets has been extensively used for statistically stationary turbulent dispersed flows.[18,19] The droplet/eddy interaction time is assumed to be the minimum of either the eddy lifetime or the droplet transit time to cross the eddy. The details of simulation procedures and various aspects associated with the interaction times can be found in Reference 6.

3. NUMERICAL MODEL

By using the operator-splitting method, the governing gas phase conservation equations can be discretized as follows.

Predictor

Momentum (u^*)

$$\left(\frac{\rho^n}{\Delta t} - A_0\right)u_i^* = H^n(u_i^*) - \Delta_i p^n + S_{u_i}^n + S_{u_i,l} + \frac{\rho^n u_i^n}{\Delta t}. \tag{4}$$

Scalar (ϕ^*)

$$\left(\frac{\rho^n}{\Delta t} - B_0\right)\phi^* = J^n(\phi^*) + S_\phi^n + S_{\phi,l} + \frac{\rho^n \phi^n}{\Delta t}. \tag{5}$$

Here the coefficient matrices A_0 and B_0 and the operators H and J contain the convective and diffusive contributions respectively. To improve the numerical stability in multiphase reacting flows, A_0 and B_0 may include the coefficient matrices resulting from the implicit treatment of the strong non-linear source terms such as chemical reaction rates, turbulence source terms and multiphase interaction source terms. The general scalar dependent variable ϕ may represent energy, mass fraction or turbulen transport quantities. At this stage the velocity field (u_i^*) does not satisfy the continuity equation. The temperature T^* is calculated from the flow field (energy, species, momentum) at the predictor step.

First corrector

Momentum (u^{**}). A new flow field (u^{**}, p^*, ρ^*) is sought to satisfy the continuity equation

$$\frac{1}{\Delta t}(\rho^* - \rho^n) + \Delta_i(\rho^* u_i^{**}) = S_{m,l}. \tag{6}$$

The discretized momentum equations are

$$\left(\frac{1}{\Delta t} - \frac{A_0}{\rho^*}\right)\rho^* u_i^{**} = H^n(u_i^*) - \Delta_i p^* + S_{u_i}^n + S_{u_i,l} + \frac{\rho^n u_i^n}{\Delta t}. \tag{7}$$

Equation (7) can be rewritten as

$$\left(\frac{1}{\Delta t} - \frac{A_0}{\rho^n}\right)\rho^* u_i^{**} + \frac{A_0}{\rho^n} u_i^{**}(\rho^* - \rho^n) = H^n(u_i^*) - \Delta_i p^* + S_{u_i}^n + S_{u_i,l} + \frac{\rho^n u_i^n}{\Delta t}. \tag{8}$$

To derive the pressure equation, the present procedure approximates the second term on the LHS of equation (8) as $(A_0/\rho^n)u_i^*(\rho^* - \rho^n)$. This approximation results in the splitting error $(A_0/\rho^n)(u_i^{**} - u_i^*)(\rho^* - \rho^n)$. Since the previous study[4] completely neglects this term, the resulting error is $(A_0/\rho^n)u_i^{**}(\rho^* - \rho^n)$, which is much bigger than the splitting error in the present formulation. Thus it is expected that the present approach can improve convergence and accuacy especially in dealing with fast transient flows as well as steady high-speed flows. Equations (6) and (8) are now used to derive the pressure equation. Taking the divergence of (8) and substituting into (6) yields

$$\left[-\frac{1}{\Delta t RT^*} + \Delta_i\left(Du^n \frac{A_0}{\rho^n}\frac{u_i^*}{RT^*}\right) + \left(Du^n \frac{A_0}{\rho^n}\frac{u_i^*}{RT^*}\right)\Delta_i + \Delta_i(Du^n \Delta_i)\right]p^*$$
$$= \Delta_i\left[Du^n\left(A_0 u_i^* + H^n(u_i^*) + S_{u_i}^n + S_{u_i,l} + \frac{\rho^n u_i^n}{\Delta t}\right)\right] - \frac{\rho^n}{\Delta t} - S_{m,l}, \tag{9}$$

where

$$Du^n = \left(\frac{1}{\Delta t} - \frac{A_0}{\rho^n}\right)^{-1}.$$

Equation (9) can be solved for the corrected pressure p^*. The density (ρ^*) is calculated from the equation of state. The velocities (u_i^{**}) are computed from (8).

Scalar (ϕ^{**}). These new flow field properties (u_i^{**}, ρ^*) satisfying the continuity equation (6) are used to update the B-coefficient:

$$\left(\frac{\rho^*}{\Delta t} - B_0^*\right)\phi^{**} = J^*(\phi^*) + S_\phi^* + S_{\phi,l} + \frac{\rho^n \phi^n}{\Delta t}. \tag{10}$$

The temperature T^{**} is calculated from the corrected flow field (energy, species, momentum).

Second corrector

Momentum (u^{***}). A new flow field (u^{***}, p^{**}, ρ^{**}) is sought to satisfy the continuity equation

$$\frac{1}{\Delta t}(\rho^{**} - \rho^n) + \Delta_i(\rho^{**} u_i^{***}) = S_{m,l}. \tag{11}$$

The discretized momentum equations are

$$\left(\frac{1}{\Delta t} - \frac{A_0^*}{\rho^*}\right)\rho^{**} u_i^{***} + \frac{A_0^*}{\rho^*} u_i^{***}(\rho^{**} - \rho^*) = H^*(u_i^{**}) - \Delta_i p^{**} + S_{u_i}^* + S_{u_i,l} + \frac{\rho^n u_i^n}{\Delta t}. \tag{12}$$

The second term on the LHS of equation (12) is similarly approximated by replacing u_i^{***} with u_i^{**}. The corresponding splitting error is $(A_0^*/\rho^*)(u_i^{***} - u_i^{**})(\rho^{**} - \rho^*)$. By taking the divergence of (12) and substituting into (11), the corrected pressure equation is obtained as

$$\left[-\frac{1}{\Delta t RT^{**}} + \Delta_i\left(Du^* \frac{A_0^*}{\rho^*}\frac{u_i^{**}}{RT^{**}}\right) + \left(Du^* \frac{A_0^*}{\rho^*}\frac{u_i^{**}}{RT^{**}}\right)\Delta_i + \Delta_i(Du^*\Delta_i)\right]p^{**}$$
$$= \Delta_i\left[Du^*\left(A_0^* u_i^{**} + H^*(u_i^{**}) + S_{u_i}^* + S_{u_i,l} + \frac{\rho^n u_i^n}{\Delta t}\right)\right] - \frac{\rho^n}{\Delta t} - S_{m,l}, \tag{13}$$

where

$$Du^* = \left(\frac{1}{\Delta t} - \frac{A_0^*}{\rho^*}\right)^{-1}.$$

Using the corrected pressure (p^{**}), the density (ρ^{**}) is obtained from the equation of state. The velocities (u_i^{***}) are computed from (12).

Scalar (ϕ^{***}). These new flow field properties (u_i^{***}, ρ^{**}) satisfying the continuity equation (11) are used to update the B-coefficient:

$$\left(\frac{\rho^{**}}{\Delta t} - B_0^{**}\right)\phi^{***} = J^{**}(\phi^{**}) + S_\phi^{**} + S_{\phi,l} + \frac{\rho^n \phi^n}{\Delta t}. \tag{14}$$

The temperature T^{***} is calculated from the updated flow field (energy, species, momentum). The updated flow-field (ρ^{**}, p^{**}, u_i^{***}, T^{***}, ϕ^{***}) is taken to represent the field values at the next time step ($n + 1$). This completes the sequence in the solution of the equation over the time step. The additional correction can be similarly implemented. The present unsteady computations are performed with one predictor and three corrector steps. Compared with the previous pressure-based methods,[20,21] this new method is more suitable for fast transient reacting flows at all speeds. For steady state calculations the present procedure can be simplified by freezing the coefficient matrices (A_0, B_0).

In the present finite volume formulation all dependent and independent variables are stored at the same grid location and the variables at the finite control volume boundaries are interpolated between adjacent grid points. To enhance the numerical stability in transient reacting flow simulations, the implicit Euler scheme is employed in differencing the temporal domain. The gas phase governing equations are discretized on a general non-orthogonal curvilinear co-ordinate system with a second-order upwind scheme[22] maintaining the TVD (total-variation-diminishing) property. If necessary, the interphase coupling between particle and gas can be handled by the same time-splitting technique.[6] Implicit coupling procedures are used to treat momentum exchanges in order to avoid small time steps. The unsteady solution procedure[6] for two-phase coupling is different from the conventional PSIC procedure[7] in which global iterations are required between two phases. The solution of the dispersed liquid droplet equations formulated on a Lagrangian frame is embedded within the non-iterative predictor–corrector solution procedure.

For the subsonic inlet boundary the entropy and the total pressure are specified. The axial velocity components are obtained by extrapolation and the vertical velocity components are determined by enforcing the vorticity to vanish at the upstream boundary. The wall was assumed to be adiabatic. At the supersonic outlet all dependent variables are extrapolated from the interior. Because of the all-speed capability of the present numerical model, a non-reflective outlet boundary condition is easily imposed. The converged steady state solution on a given grid is used as an initial condition for the unsteady computation. The transient solution is initiated by perturbing the steady state inlet pressure fields with an m^{th} longitudinal mode for several cycles:

$$p(0, y, t) = \bar{p}(0, y, 0)[1 + C_{\text{pert}} \cos(\omega_m t)]. \tag{15}$$

Here $\bar{p}(0, y, 0)$ and C_{pert} are the steady inlet pressure and the perturbation constant respectively. The initial perturbed density and temperature are calculated using the isentropic relations.

4. RESULTS AND DISCUSSION

In this section we present the results of the present pressure-based method for the shock-tube problem, an axisymmetric blast flow field problem and fast transient spray-combusting flows.

Figure 1 shows the dimensions and related initial conditions for the shock-tube problem. A diaphragm located at the centre of the tube separates gas in a low-pressure chamber from gas in a high-pressure chamber. With rupture of the diaphram at $t = 0$ the resulting flow is characterized by the presence of a shock wave, a contact discontinuity and a rare faction wave. Computations are based on a 200 uniform grid. Figures 2 and 3 show the profiles for velocity and density at time $t = 0{\cdot}05$ for two different time intervals. In this figure PISO 1 represents a solution technique suggested by Issa *et al.*[4] and PISO 2 denotes the method proposed in the present study. As expected, the larger time interval considerably increases the phase error and

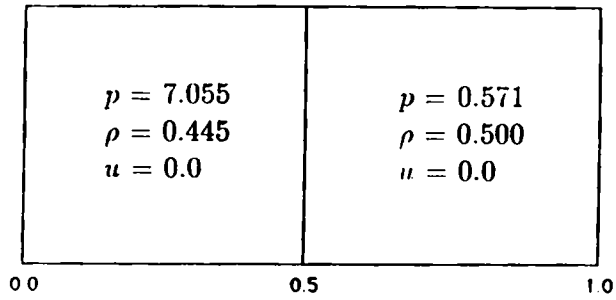

Figure 1. Schematic of shock-tube problem

the discontinuity smearing. In the velocity profiles with the larger time interval ($\Delta t = 2.0 \times 10^{-3}$ s) the numerical results from PISO 2 show a better agreement with the exact solution. Because of the larger temporal splitting error associated with PISO 1, deviations are large in the high-velocity flow region. Upon increasing the computational time step to $\Delta t = 2.5 \times 10^{-3}$ s, the PISO 1 solution procedure diverges while the solution can still be obtained with PISO 2. It is quite possible that the large splitting error associated with PISO 1 causes the velocity–pressure decoupling for high-velocity flow calculations with relatively large time step. These numerical

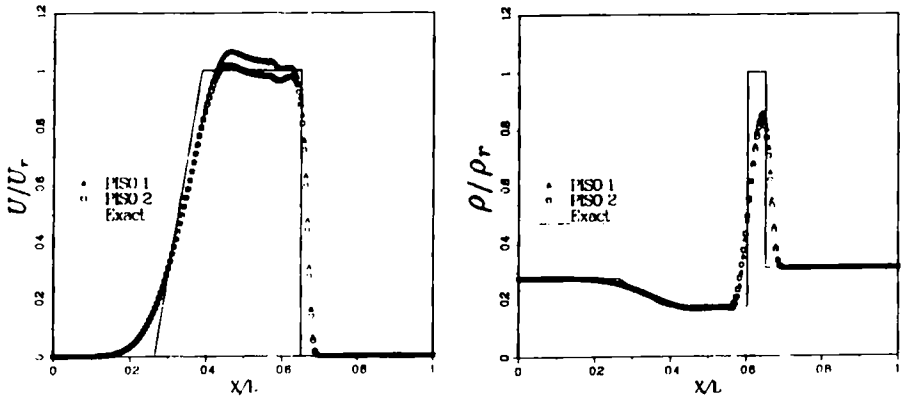

Figure 2. Profiles for velocity and density ($\Delta t = 2{\cdot}0 \times 10^{-3}$, $U_r = 2{\cdot}074$, $\rho_r = 1{\cdot}598$)

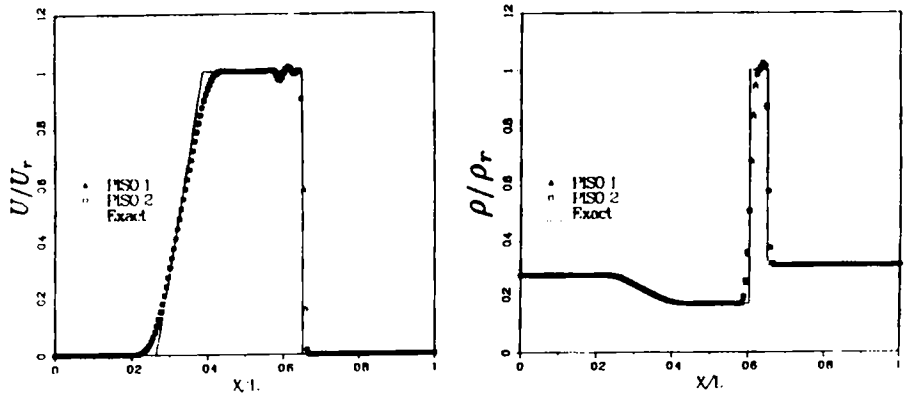

Figure 3. Profiles for velocity and density ($\Delta t = 3{\cdot}3 \times 10^{-4}$, $U_r = 2{\cdot}074$, $\rho_r = 1{\cdot}598$)

results suggest that PISO 2 is more suitable for fast transient flows and high-speed steady flows. In the predicted profiles with the smaller time interval ($\Delta t = 3.3 \times 10^{-4}$ s) PISO 1 and PISO 2 predict almost identical solutions owing to the reduced splitting error. As shown in Figure 3, the present pressure-based method predicts well the main features of the solution, namely an expansion wave propagating to the left high-pressure side and a shock wave, followed by a contact discontinuity, propagating to the right low-pressure side. However, noticeable overshoots and undershoots exist for the velocity profile near the contact discontinuity and the shock front. The slightly oscillatory velocity profiles close to the high-gradient regions are linked with the underpredicted or overpredicted density due to the certain level of discontinuity smearing predicted by the present pressure-based method. These could be related to the upwinding procedure of the pressure-based method, which is based on one physical velocity rather than three characteristic velocities in context with the density-based method. Nevertheless, the numerical results indicate that the present pressure-based method has the ability to predict the wave speed and the overall shock structure correctly. Even though the accuracy of the present pressure-based method is not as good as the accuracy of the high-resolution density-based method,[23] the present pressure-based method can be used for the prediction of the combustion instability phenomena which mostly occur in low-Mach-number reacting flow regions. In addition, the prediction capability of the pressure-based method could be improved by utilizing higher-order spatial and temperal discretization and further refinement of the sequential solution procedure.

The next example problem is the blast flow field generated by an open-ended axisymmetric shock-tube. Initial conditions and basic dimensions are described in Figure 4. A blast wave, followed by an imbedded Mach disc, propagates downstream into a quiescent sea-level open space at the design shock speed $Ma = 1{\cdot}75$. In the subsonic flow region behind the shock a rarefaction wave propagates into the tube. Air viscosity is considered in this calculation. Computations are performed using a 100×70 non-uniform grid and a non-dimensional time interval of 0·01. Figure 5 shows the pressure time history at a location of $X/D = 1.51$ on the centreline. At $t < 1{\cdot}2$ ms the numerical results agree well with the experimental data[24] in terms of the pressure time rise and the pressure variations after the blast wave past the pressure probe. After $t = 1{\cdot}2$ ms the measured pressure data are unreliable owing to the interference of the pressure probe with the Mach disc moving downstream. Figure 6 shows the contours of predicted density and pressure field at $t = 0{\cdot}75$ and $1{\cdot}50$ ms. In comparison with the experimental shadowgraph picture[24] at $t = 1{\cdot}50$ ms, the present solution algorithm correctly predicts the main

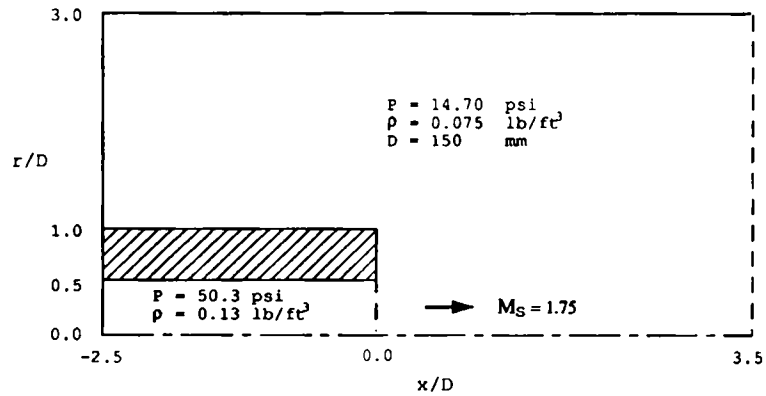

Figure 4. Initial conditions and dimensions for axisymmetric blast flow field problem

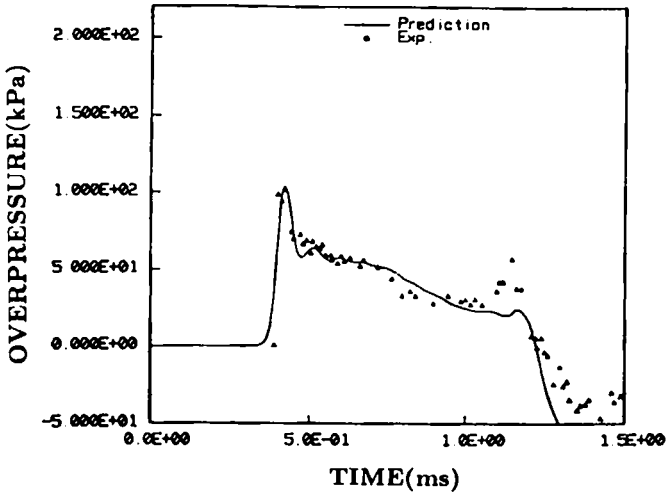

Figure 5. Comparison of predicted and measured overpressure time history at $X/D = 1{\cdot}51$

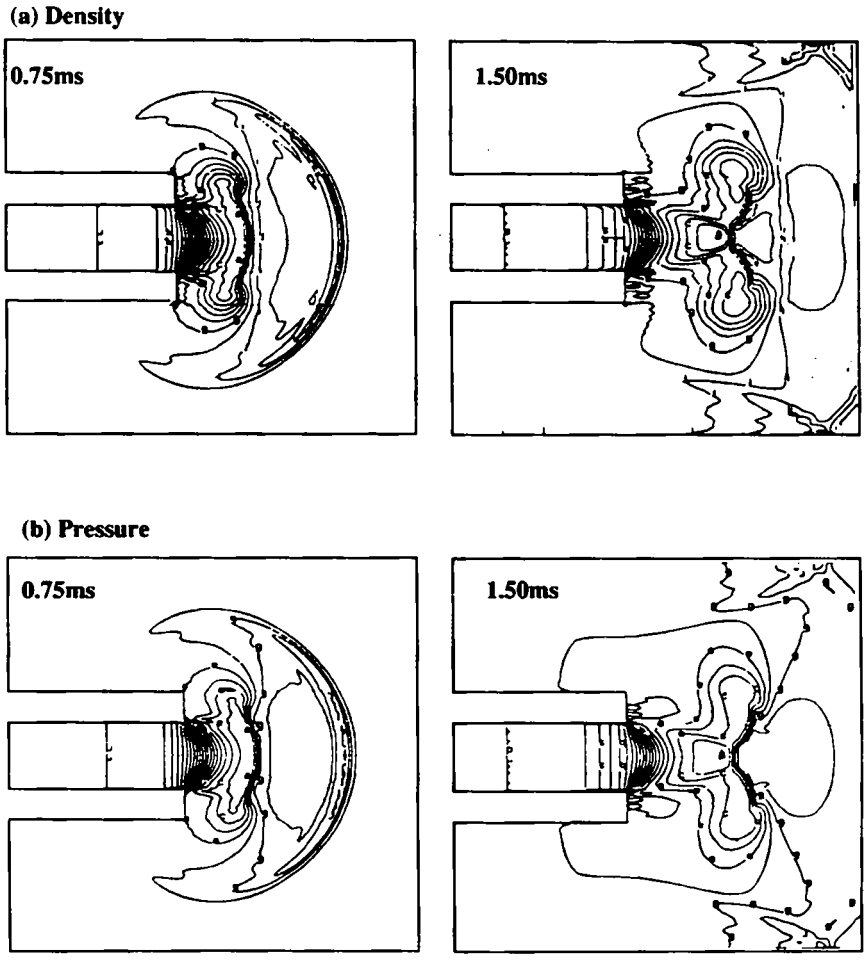

Figure 6. Contours of density and pressure at $t = 0{\cdot}75$ and $1{\cdot}50$ ms

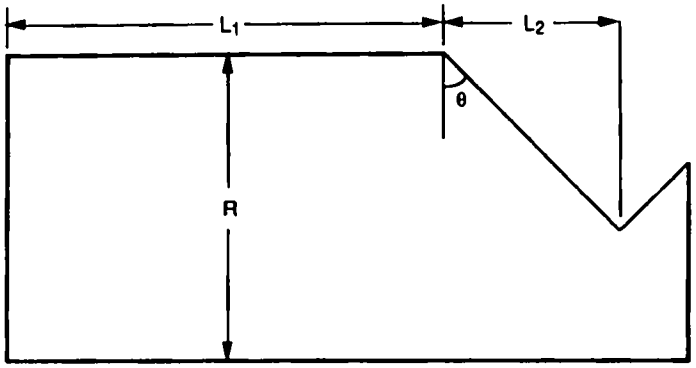

Figure 7. Geometry of liquid-fuelled rocket engine

features of the complicated blast flow field, including the Mach disc, the jet shock, the recompression shock, the triple point, the vortex above the Mach disc and the embedded shock upstream of the vortex.

Finally, the present pressure-based method is applied to predict the stability characteristics and fast transient spray-combusting flows in liquid-fuelled rocket engines as shown in Figure 7. The basic dimensions of this combustor are the same as those of the Space Shuttle main engine. However, the actual engine geometry is simplified for the parametric study on combustion instability. Detailed dimensions of three investigated engines are listed in Table I. In the actual rocket thrust chamber, liquid reactants are atomized and vaporized and the entire mixture is combusted within the combustion chamber. The reaction products are expanded through a converging–diverging nozzle which has subsonic, transonic and supersonic flow zones. In the preliminary stage of the CFD-based instability analysis for the rocket thrust chamber we neglect supercritical vaporization effects and dense spray processes such as atomization, drop break-up and drop coalescence. Tetradecane was used as the fuel and monodisperse droplets are injected at 10 equally spaced injectors. The injection velocity is $10\ \mathrm{m\ s^{-1}}$ and the initial droplet temperature is 300 K. Investigated parameters include the initial droplet size, the equivalence ratio and the combustor geometry (combustor length and nozzle length in converging section). Computed cases were chosen to cover a wide range of operating conditions: droplet radii of 50, 70, 100, 120 and 150 μm, fuel equivalence ratios of 0·65 and 1·3, and combustor geometries of E_1, E_2 and E_3. Calculations were performed on a 65 × 37 grid with a time interval of $\Delta t = 5{\cdot}0 \times 10^{-5}$ s in all cases.

The effects of droplet size on combustion instability are shown in Figures 8–10. At the equivalence ratio of 1·3 with engine E_1 the initial droplet size $r_{k,0} = 100$ μm produces an unstable engine condition, while the smaller and larger droplet sizes $r_{k,0} = 50$ and 150 μm respectively yield stable engine conditions. The smaller initial droplet size ($r_{k,0} = 50$ μm) results in a higher vaporization rate near the injector, an increase in gas temperature, a more efficient combustion

Table I. Dimensions of liquid-fuelled rocket engines

Engine	L_1 (m)	L_2 (m)	R (m)	R_t (m)	Θ (deg)
E_1	0·3534	0·2094	0·2266	0·1309	65·44
E_2	0·1767	0·2094	0·2266	0·1309	65·44
E_3	0·1767	0·1047	0·2266	0·1309	47·57

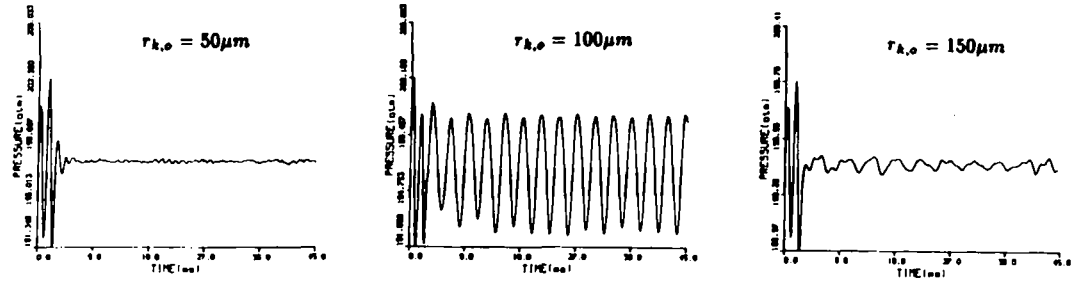

Figure 8. Pressure oscillations for three initial spray conditions (ϕ = 1·3, C_{pert} = 0·02, X/L_1 = 0·0, Y/R = 0·5, E_1)

Figure 9. Spray parcel distribution for three initial spray conditions (ϕ = 1·3, C_{pert} = 0·02, E_1)

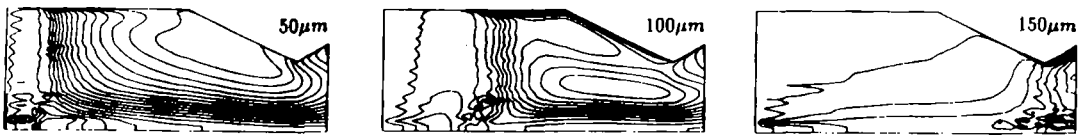

Figure 10. Contours of temperature for three initial spray conditions (ϕ = 1·3, C_{pert} = 0·02, X/L_1 = 0·0, E_1)

and a stable engine condition. The larger initial droplet size ($r_{k,0}$ = 150 μm) results in a lower evaporation rate, a decrease in gas temperature, an increased exit flow rate of unburned liquid fuel and a stable engine condition. Owing to the increase in escaped liquid fuel, the acoustic energy fed back by combustion is not enough to sustain the combustion instability. For the initial drop size $r_{k,0}$ = 100 μm the spray combustion process becomes unstable. In this unstable range of the droplet radii the overall combustion time lag dominantly influenced by the droplet heat-up period matches with the acoustic time scale and the resulting flow oscillations appear as the unstable motion of a self-excited system. In other words, if there is no exit flow rate for the unburned liquid fuel, the more widely distributed evaporation rate corresponding to the larger initial droplet size can provide sufficient energy to sustain the acoustic longitudinal mode oscillations. In general the oscillatory response characteristics depend on the overall combustion time scale and the acoustic time scale. The overall combustion time scale may be contributed to by the droplet heat-up period, the ignition delay time, the turbulent mixing time scale and the time scale associated with atomization. The acoustic time scale depends on the combustor length, the equivalence ratio, the initial spray conditions and the nozzle acoustic admittance. The combustor becomes unstable when the overall combustion time scale is close to the acoustic time scale; therefore the oscillation response characteristics could be avoided by widely separating the acoustic time scale and the overall combustion time scale.

To investigate the unsteady behaviour of the fast transient spray-combusting flow field in detail, one unstable case is selected. Figure 11 shows the transient and cycle flow oscillations for $r_{k,0}$ = 120 μm and ϕ = 1·3. For this initial droplet size it can be seen that the combustion

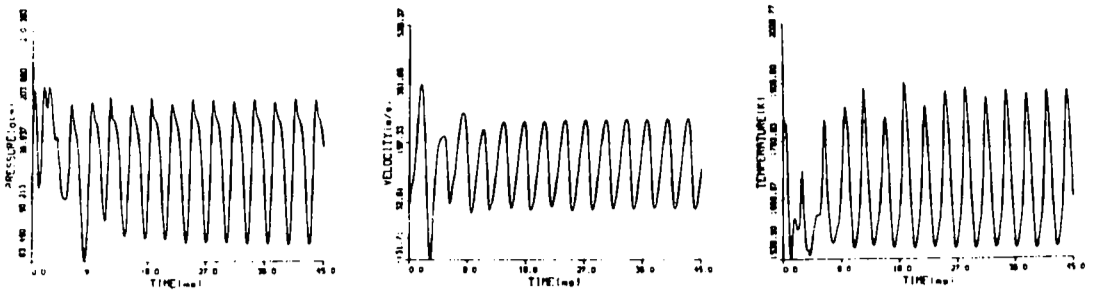

Figure 11. Flow oscillations of pressure, velocity and temperature ($r_{k,0} = 120\,\mu$m, $\phi = 1{\cdot}3$, $C_{pert} = 0{\cdot}02$, $X/L_1 = 0{\cdot}0$, $Y/R = 0{\cdot}5$, E_1)

becomes highly unstable. These numerical results suggest that at this initial droplet size with the equivalence ratio of 1·3 the time lag associated with the droplet heat-up period matches with the acoustic time scale and the resulting flow oscillations appear as the unsteady motion of a self-excited system. Figure 12 shows the spray parcel distribution and temperature contours during one limiting cycle shown in Figure 11. In this figure $t = 27{\cdot}0$ ms corresponds to the end of the expansion cycle (starting point of compression near the injector face), $t = 27{\cdot}4$ ms to about the middle of compression, $t = 27{\cdot}8$ ms to the end of compression, $t = 28{\cdot}9$ ms to the middle

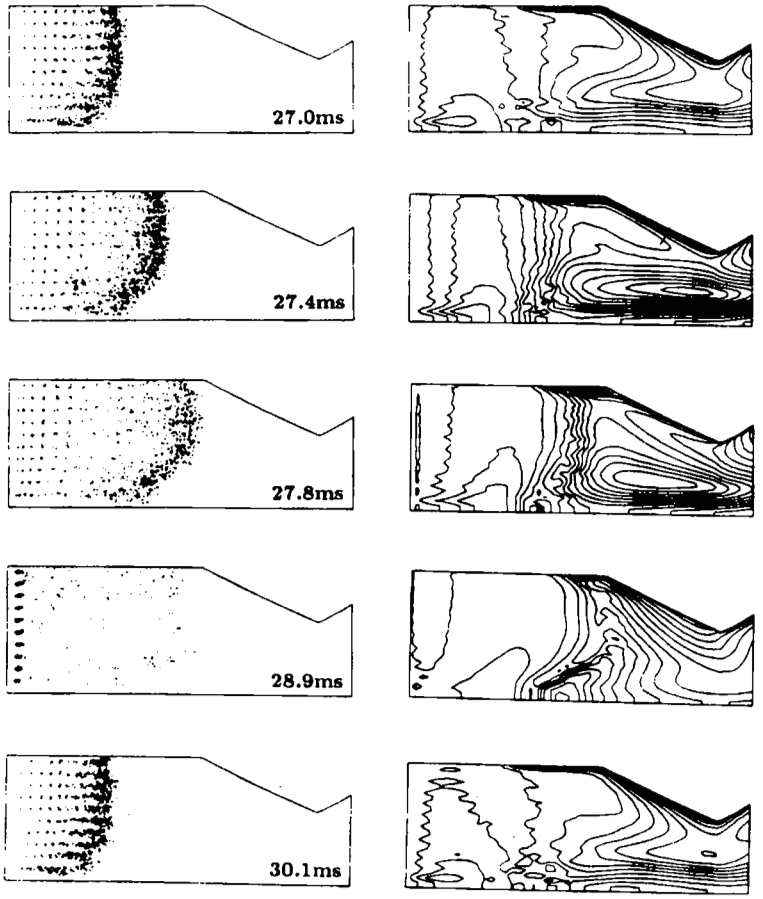

Figure 12. Spray parcel distribution and temperature contours ($r_{k,0} = 120\,\mu$m $\phi = 1{\cdot}3$, $C_{pert} = 0{\cdot}02$, E_1)

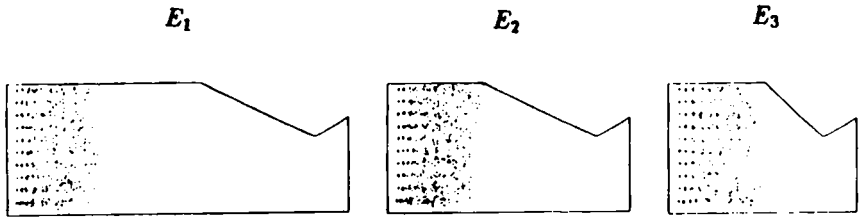

Figure 13. Spray parcel distribution for three engines ($r_{k,0} = 100\ \mu m$, $\phi = 0{\cdot}65$, $C_{pert} = 0{\cdot}02$, $Y/R = 0{\cdot}5$)

of expansion and $t = 30{\cdot}1$ ms to the end of expansion. At $t = 27{\cdot}0$ ms the pressure and temperature are at about their lowest values and the velocity is about its highest value. The corresponding relative velocity is very high near the injector and the resulting interval of spray parcels is at about the maximum level. Most vaporization occurs at $0{\cdot}4 \leq X/L_1 \leq 0{\cdot}6$ and the hot combustion zone is located around $X/L_1 = 0{\cdot}55$. When the compression continues, the fuel spray reaches the more downstream region and the vaporization rate is widely distributed. The resulting hot combustion zone is located in a more downstream region. The present N-type wave during the limiting cycle has a very short compression period (0·8 ms) and a long expansion period (2·3 ms). At the early stage ($t = 28{\cdot}9$ ms) of the expansion cycle the spray parcels are closely located near the injector, because the relative velocity and gas velocity are very low. This low relative velocity and low gas velocity result in the accumulation of fuel sprays near the injector and the uniform distribution of vaporization in the downstream region. When the expansion continues, the velocity increases and the accumulated spray parcel starts to separate. At the end of the expansion the cycle returns to the starting point of the compression cycle ($t = 30{\cdot}1$ ms).

Figures 13 and 14 show the steady state spray parcel distribution and pressure oscillations for all three engines (E_1, E_2, E_3). We select the initial drop size $r_{k,0} = 70\ \mu m$ which yields a stable condition for E_1. For E_2 and E_3 the dimensions L_1 and L_2 are changed while maintaining the same dimensions for the chamber radius and throat radius. To check the effects of combustor length and acoustic time scale on combustion instability, the combustor length (L_1) of E_2 is taken as the half-length of E_1. The flow oscillations for E_2 appear weakly unstable and its peak-to-peak pressure amplitude at the nozzle entrance is about 3·1 atm. This trend is quite different from previous one-dimensional studies[25,26] with a short-nozzle boundary condition, which yield stability characteristics sensitive to the combustor length owing to the lower nozzle damping. To check the effects of nozzle length (L_2) and nozzle acoustic admittance, the nozzle length (L_2) of E_3 is taken as the half-length of E_2. The resulting flow oscillations for E_3 appear

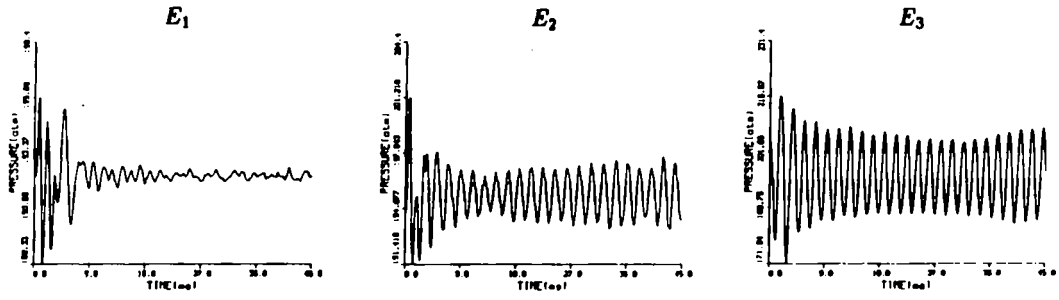

Figure 14. Pressure oscillations for three engines ($r_{k,0} = 100\ \mu m$, $\phi = 0{\cdot}65$, $C_{pert} = 0{\cdot}02$, $Y/R = 0{\cdot}5$)

strongly unstable and its peak-to-peak pressure amplitude at the nozzle entrance is 28·3 atm. These numerical results indicate that the combustion stability characteristics are more sensitive to the nozzle length than to the combustor length. By decreasing the effective combustor length, the fundamental acoustic frequencies in the unstable engine increase (520 Hz for E_2, 560 Hz for E_3).

It is necessary to note that the present numerical model with a subcritical vaporization process cannot capture all physical phenomena, especially in the high-pressure situation where supercritical vaporization is dominant. However, thhe supercritical vaporization model is still in the development stage.[27] Only an *ad hoc* supercritical vaporization model was implemented in the CFD code.[28] In high-pressure environments dense spray effects such as droplet break-up and the atomization process may dominantly effect the vaporization time scale. Future work must include the incorporation of physical processes such as atomization, stream and droplet break-up and vaporization under supercritical conditions.

5. CONCLUSIONS

The present pressure-based method has successfully demonstrated its capability to predict combustion instability in liquid-fuelled engines as well as fast transient compressible flows at all speeds. Numerical results indicate that droplet vaporization processes as well as the combustor geometry play a crucial role in releasing thermal energy and driving the combustion instability. To improve the predicative capability for non-linear combustion instability, it is necessary to incorporate physical submodels which can link all relevant physical phenomena of the entire liquid propellant combustion process.

ACKNOWLEDGEMENTS

This work has been partially supported by Cray Research Inc. (University R & D Grant Program). The authors also wish to acknowledge the Cray X-MP CPU time supplied by the Alabama Supercomputer Network through the University of Alabama in Huntsville.

REFERENCES

1. Y. M. Kim, C. P. Chen, J. P Ziebarth and Y. S. Chen, 'Prediction of high frequency combustion instability in liquid propellant rocket engines'. *AIAA Paper 92-3763*, 1992.
2. H. Q. Yang, M. Z. Pindera, A. J. Przekwas and K. Tucker, 'A study of pressure-based methodology for resonant flows in non-linear combustion instabilities'. *AIAA Paper 92-0779*, 1992.
3. S. Thakur and W. Shyy, 'Development of high accuracy convection schemes for sequential solvers'. *Numerical Heat Transfer*, in press.
4. R. I. Issa, B. Ahmadi-Befrui, K. R. Beshay and A. D. Gosman, 'Solution of the implicitly discretized reacting flow equations by operator-splitting'. *J. Comput. Phys.*, **93**, 388–410 (1991).
5. T. D. Butler and P. J. O'Rourke, 'A numerical method for two dimensional unsteady reacting flows'. *Proc. 16th Symp. on Combustion*, 1976, pp. 1503–1515.
6. C. P. Chen, H. M. Shang and Y. Jiang, 'A novel gas–droplet numerical method for spray combustion'. *Int. j. numer. methods fluids*, **15**, 233–245 (1992).
7. C. T. Crowe, M. P. Sharma and D. E. Stock. 'The particle source in cell method for gas–droplet flows'. *J. Fluids Eng.*, **99**, 325 (1977).
8. L. D. Cloutman, J. K. Dukowicz, J. D. Ramshaw and A. A. Amsden, 'CONCHAS-SPRAY: a computer code for reactive flows with fuel sprays'. *Los Alamos National Laboratory Rep. LA-9294-MS*, 1982.
9. Y. El Banhawy and J. M. Whitelaw, 'Calculation of the flow properties of confined kerosene-spray flames'. *AIAA J.*, **18**, 1503–1510 (1980).
10. W. P. Jones, 'Models for turbulent flows with variable density and combustion', in W. Kollman (ed.), *Prediction Method for Turbulent Flows*. Hemisphere, London, 1980, pp. 379–422.
11. B. F. Magnussen and B. H. Hjertager, 'On mathematical modeling of turbulent combustion with special emphasis on soot formation and combustion'. *Proc. 16th Symp. on Combustion*, 1976, p. 719.
12. C. K. Westbrook and F. L. Dryer, 'Chemical kinetic modelling of hydrocarbon combustion'. *Prog. Energy Combust. Sci.*, **10**, 1–57 (1984).

13. N. Frossing, 'On the evaporation of falling droplets'. *Gerl. Beltr. Geophys.*, **52**, 170–216 (1938).
14. B. Abramzon and W. A. Sirignano, 'Droplet vaporization model for spray combustion calculations'. *AIAA Paper 88-0636*, 1988.
15. W. A. Sirignano, 'Fuel droplet vaporization and spray combustion'. *Prog. Energy Combust. Sci.*, **9**, 291–322 (1983).
16. G. L. Hubbard, V. E. Denny and A. F. Mills, 'Droplet vaporization: effects of transient and variable properties'. *Int. J. Heat Mass Transfer*, **18**, 1003–1008 (1975).
17. D. R. Stull and H. Prophet, *JANAF Thermochemical Tables*, 2nd edn, 19XX; N. W. Chase *et al.*, *J. Phys. Chem. Ref. Data*, **3**, 311 (1974).
18. A. D. Gosman and E. Ioannides, 'Aspects of computer simulation of liquid fueled combustors'. *AIAA Paper 81-0323*, 1981.
19. A. Fashola and C. P. Chen, 'Modeling of confined turbulent fluid–particle flows using Eulerian and Lagrangian schemes.' *Int. J. Heat Mass Transfer*, **33**, 691–700 (1990).
20. R. I. Issa, 'Solutions of the implicitly discretized fluid flow equations by operator splitting'. *J. Comput. Phys.*, **62**, 40–65 (1985).
21. C. P. Chen, Y. Jiang, Y. M. Kim and H. M. Shang, 'MAST—a multi-phase all-speed transient Navier–Stokes code in generalized coordinates'. *NASA Contract Rep. NAGS-092*, 1991.
22. S. R. Chakravarthy and S. Osher, 'A new class of high accuracy TVD schemes for hypersonic conservation laws'. *AIAA Paper 85-0363*, 1985.
23. P. Colella and P. R. Woodward, 'The piecework parabolic method (PPM) for gas dynamical simulations'. *J. Comput. Phys.*, **54**, 174–201 (1984).
24. J. C. T. Wang and G. F. Widhopf, 'A high-resolution TVD finite volume scheme for the Euler equations in conservation form'. *J. Comput. Phys.*, **84**, 145–173 (1989).
25. R. Bhatia and W. A. Sirignano, 'A one-dimensional model of ramjet combustion instability'. *AIAA Paper 90-0271*, 1990.
26. Y. M. Kim, C. P. Chen and J. P. Ziebarth, 'Vaporization effects on combustion instability of liquid-fueled engines'. *Fifth Int. Conf. on Liquid Atomization and Spray Systems (ICLASS-91, Poster Session)*. Washington, DC, July 1991.
27. V. Yang, C. C. Hsiao and J. S. Shuen, 'Pressure-coupled vaporization and combustion responses of liquid fuel droplets in high-pressure environments', *AIAA Paper 91-2310*, 1991.
28. P. Y. Liang and R. J. Jensen, 'Modeling of dense sprays from LOX/H2 coaxial injectors under supercritical conditions'. *Proc. 22nd JANAF Combustion Meet.*, October 1985.